NUMERICAL SIMULATION RESEARCH ON TWO-PHASE FLOW MOTION AND HEAT DISTRIBUTION CHARACTERISTICS IN EPIDEMIC PREVENTION SURVEILLANCE VEHICLES

by

Enhai LIU[a], Gengyang CHEN[a], Xiaoyong WEI[b*], Siting YANG[a], Mingguo PENG[a*], Biaocai BAI[a], and Yine JIANG[a]

[a] Changzhou University, Changzhou, China
[b] Bergstrom (Changzhou) Heat Exchangers Co., Ltd., Changzhou, China

Original scientific paper
https://doi.org/10.2298/TSCI2602017L

The dynamics of two-phase flow and the thermal distribution characteristics within an epidemic prevention surveillance vehicle exert a profound influence on the risk of cross-infection among occupants and their comfort levels. In this study, numerical simulation techniques are employed to comprehensively analyze the two-phase flow motion and thermal distribution characteristics inside the vehicle. Specifically, the research explores the impact of modular temperature and humidity control on two-phase flow behavior and spatial thermal distribution. The findings indicate that the maximum aerosol concentration recorded was 7.2×10^{-17} $\mu g/m^3$ at a height of 1.5 m above the vehicle floor. Additionally, as the temperature rises, the intensity of the two-phase flow motion concomitantly increases, while the level of humidity exhibits an inverse trend. From the perspective of in-vehicle comfort, the modular temperature and humidity zoning control approach contributes to a more homogeneous distribution of air velocity and temperature within the epidemic prevention surveillance vehicle. Consequently, this configuration offers an augmented level of thermal comfort for both medical personnel and patients.

Keywords: *monitoring vehicle, two-phase flow, modular zoning, thermal distribution characteristics*

Introduction

At the conclusion of 2019, the novel strain of coronaviruses (SARS-CoV-2) that causes the disease known as SARS-CoV-2 had spread rapidly across the globe, posing an unprecedented challenge to countries worldwide [1-3]. In response to this public health emergency, nations have implemented strict epidemic prevention measures. Vehicles play a pivotal role in the execution of tasks and the assurance of the well-being and security of medical and monitoring personnel. The vehicle air conditioning system primary function is to regulate temperature and humidity levels within the cabin, as well as to purify the air. The effectiveness of this system directly impacts the comfort level experienced by passengers within the vehicle. Wan *et al.* [4] constructed a physical model of the vehicle cabin and subsequently analyzed the temperature characteristics and thermal comfort of the cabin. Zhang *et al.* [5] conducted a simulation of the 3-D temperature distribution within the cabin during the air condi-

* Corresponding authors, e-mail: liuenhai@cczu.edu.cn; jdcx1018@163.com

tioning cooling process. Aerosol particles carrying viruses are more easily transmitted in enclosed spaces. Luo *et al.* [6] employed CFD to simulate the transport process of aerosols and conducted a thorough analysis of the specific reasons for the cross-infection of the novel coronavirus within vehicles. Yang *et al.* [7] conducted a systematic study on the transport and deposition mechanisms of aerosols in vehicles through numerical simulation. The proposed vehicle air conditioning system is designed to address the specific requirements for epidemic prevention. It incorporates a clear delineation of the vehicle into vaccination and observation areas. The study utilizes numerical simulation to optimize the layout of the refrigerant pipes. The study methodically investigates the impact mechanism of fin height and fin spacing on aerosol dispersion behavior.

Design of air conditioning system in epidemic prevention vehicles

The air conditioning system for epidemic prevention vehicles

The present article proposes a novel design for an epidemic prevention monitoring vehicle-mounted hybrid refrigeration cycle system with a jet. The objective of this design is to achieve independent regulation of different functional areas within the carriage, such as the vaccination area and the observation area, in order to meet individual needs. The system utilizes R134a as the circulating working fluid. Preliminary design calculations indicate that the thermal load of the epidemic prevention monitoring vehicle system is approximately 4847 W, and its cooling capacity is estimated to be around 5332 W. The epidemic prevention vehicle air conditioning system is illustrated in fig. 1.

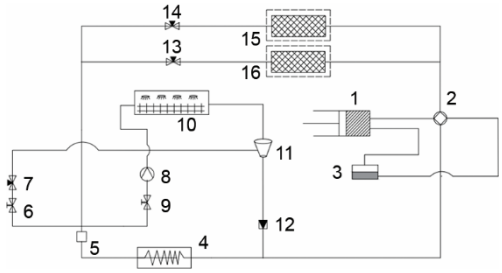

Figure 1. The air conditioning system for epidemic prevention vehicles; *1 – compressor, 2 – four-way valve, 3 – gas-liquid separator, 4 – condenser, 5 – temperature sensor bulb, 6 – control valve, 7 – loop throttle valve, 8 – circulating pump, 9 – control valve, 10 – heat generator, 11 – ejector, 12 – check valve, 13 – zone I throttle valve, 14 – zone II throttle valve, 15 – zone I heat exchanger, 16 – zone II heat exchanger*

The refrigerant is compressed into a high-temperature and high-pressure state by the primary compressor – 1. Subsequently, the liquid enters the condenser – 4 via the four-way valve – 2. In this section, the liquid undergoes dissipation, transforming into a high temperature and high pressure liquid refrigerant. Thereafter, the fluid traverses the temperature-sensitive package – 5, where it undergoes a division into three distinct pathways. One such path traverses the primary circulation system, passing through the primary throttling valves – 13 and 14 for pressure reduction, and subsequently entering the evaporators – 15 and 16 (heat exchangers for zones I and II). In these evaporators, the refrigerant undergoes a phase transition, converting into a low temperature and low pressure gaseous state. Subsequently, it reverts to the main compressor for subsequent cycles. An alternative pathway traverses the auxiliary circulation system, wherein the refrigerant, facilitated by the control valve – 9, is throttled by the loop throttling valve – 7 and enters the ejector – 11. Conversely, the third path enters the heat generator – 10 through the circulation pump – 8. In this sequence, residual heat is absorbed, gas injection is entrained, and the mixture is combined with the primary circulation refrigerant before entering the condenser – 4. This completes the refrigeration cycle.

Model construction

The objective of this study was to investigate the two-phase flow motion and thermal distribution characteristics in epidemic prevention monitoring vehicles. To this end, a physical model of the epidemic prevention carriage and a microchannel heat exchanger was constructed, as shown in fig. 2. The carriage is divided into two areas: The area demarcated as Area 1 is the designated vaccination area, and the area designated as Area 2 is the observation area. A buffer zone has been established between Area 1 and Area 2. As illustrated in fig. 3(a), the physical model of the microchannel heat exchanger is presented. Figure 3(b) provides a detailed representation of the local mesh of the heat exchanger.

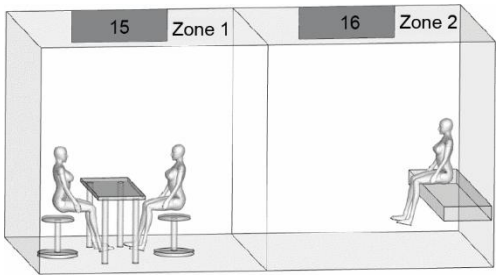

Figure 2. Model of the carriage

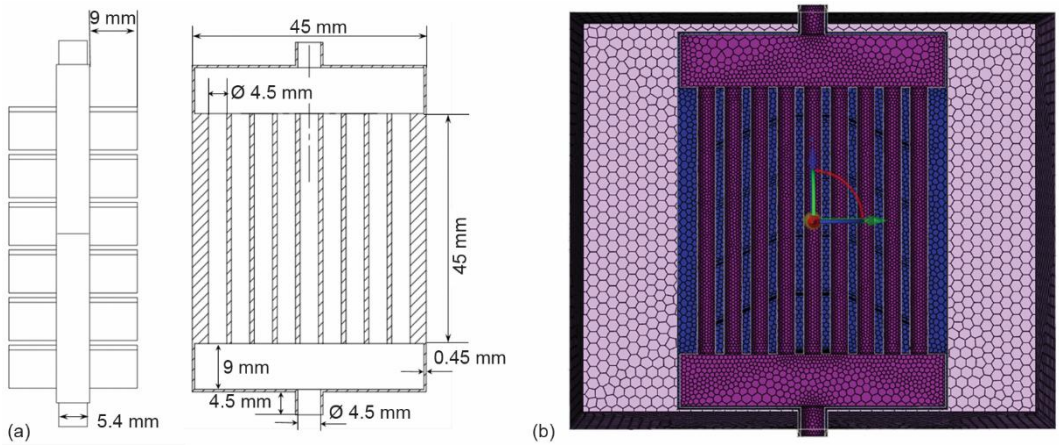

Figure 3. (a) Model of heat exchanger and (b) detail of local mesh division

As illustrated in fig. 3(b), the local mesh is meticulously delineated, and to ensure the accuracy of numerical simulations, mesh independence is evaluated using the grid convergence index (*GCI*) prior to conducting the numerical simulation [8-10]. It is imperative to define the characteristic size of the grid. The characteristic size, *h*, of the 3-D grid can be expressed:

$$h = \left[\frac{1}{N} \sum_{i=1}^{N} \Delta V_i \right]^{1/3} \tag{1}$$

where N is the number of grids within the computational domain and ΔV_i – the volume.

Calculate the error of key variables in simulation:

$$e_a^{21} = \left| \frac{f_1 - f_2}{f_1} \right| \tag{2}$$

The *GCI* is used to evaluate the discretization error independent of the grid, and the equation for calculating the *GCI* is:

$$GCI^{21} = \frac{F_s e_a^{21}}{r^p - 1} \tag{3}$$

where f_1 and f_2 are key values of the calculation results from different grids, F_s – the safety factor, p – the order, and the order of calculation accuracy is set to $p = 2$ based on experience.

In this study, 20 points were taken along the vertical line at the air inlet, representing the average velocity at 20 monitoring points. The simulation results indicate that grid computing meets the convergence criteria.

Numerical simulation

Calculation of operating conditions

The numerical calculation method is employed to select typical pipe types (circular, square, and hexagonal) for structural design, with the objective of systematically exploring the potential effects of different geometric shapes on fluid dynamics characteristics and heat transfer efficiency.

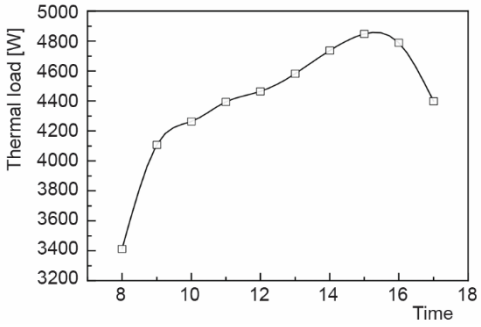

Figure 4. Total thermal load of epidemic prevention vehicles at different time periods

As demonstrated in fig. 4, within the time frame of 8-9 hours, the thermal load inside the epidemic prevention vehicle exhibited a marked increase, from 3412-4107 W, representing a 20% rise. Subsequently, during the period from 9-14 hours, the growth rate of the thermal load inside the vehicle was relatively stable. At the 15th hour, the thermal load inside the vehicle was measured at 4847 W. Subsequent to that occurrence, a downward trend was observed in the thermal load within the vehicle during subsequent time periods.

Control equations

When particles move in the air, they are affected by a variety of forces, including gravity, drag force, buoyancy, thermophoretic force, and Saffman lift force. The present study utilizes the technique of Lagrange equations to predict the trajectory of particle motion. Furthermore, the particle and air-flow are bidirectionally coupled, and the force equation for particles is [11]:

$$m_d \frac{du_d}{dt} = V_d \frac{g(\rho_d - \rho)}{\rho_d} + F_{drag} + F_x \tag{4}$$

where m_d is the mass of the droplet, u_d – the velocity of the droplet particles, V_d – the volume of the droplet, g – the acceleration due to gravity, ρ_d – the density of the droplet, ρ – the density of air, F_{drag} – the drag force acting on the droplet, and F_x – the thermophoretic force and Saffman lift force acting on the droplet.

The control equation model of micro-channel parallel flow heat exchangers typically involves the fundamental equations of fluid mechanics and heat transfer, including the continuity equation:

$$\frac{\partial u_x}{\partial x}+\frac{\partial u_y}{\partial y}+\frac{\partial u_z}{\partial z}=0 \tag{5}$$

where u_x, u_y, and u_z are the velocities in the x-, y-, and z-directions, respectively.

Momentum conservation equation:

$$\frac{\partial}{\partial x_j}(\rho u_i u_j)=-\frac{\partial P}{\partial x_j}+\rho g+\frac{\partial}{\partial x_j}\left[(\mu+\mu_i)\frac{\partial \mu_j}{\partial \mu_j}\right] \tag{6}$$

$$\frac{\partial}{\partial y_j}(\rho u_j u_j)=-\frac{\partial P}{\partial y_j}+\rho g+\frac{\partial}{\partial y_j}\left[(\mu+\mu_i)\frac{\partial \mu_j}{\partial \mu_j}\right] \tag{7}$$

$$\frac{\partial}{\partial z_j}(\rho u_i u_j)=-\frac{\partial P}{\partial z_j}+\rho g+\frac{\partial}{\partial z_j}\left[(\mu+\mu_i)\frac{\partial \mu_j}{\partial \mu_j}\right] \tag{8}$$

where P is the pressure on the surface of the fluid element, ρ – the fluid density, and g – the acceleration due to gravity. Energy conservation equation:

$$\frac{\partial}{\partial x_j}\left(\rho u_i c_p T\right)=\frac{\partial}{\partial x_i}\left(\lambda\frac{\partial T}{\partial x_i}\right)+\Phi \tag{9}$$

where c_p is the specific heat capacity, T – the temperature, λ – the thermal conductivity, and Φ – the energy diffusion equation.

Results and discussion

Characteristics of spatial contamination in epidemic prevention vehicles

To ensure adequate air circulation and prevent external contamination, an air curtain device is installed at the door position. Figure 5 illustrates the characteristics of aerosol spatial distribution within the epidemic prevention vehicle. Figure 6 illustrates the variation of aerosol concentration in space with altitude under specific conditions.

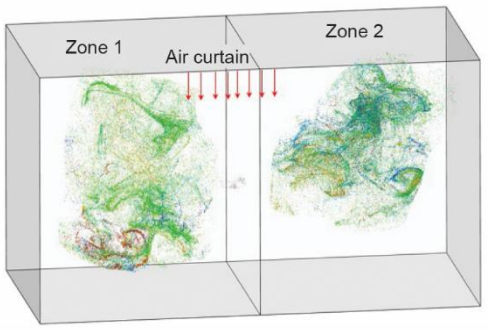

Figure 5. Characteristics of aerosol spatial distribution in the epidemic prevention vehicle

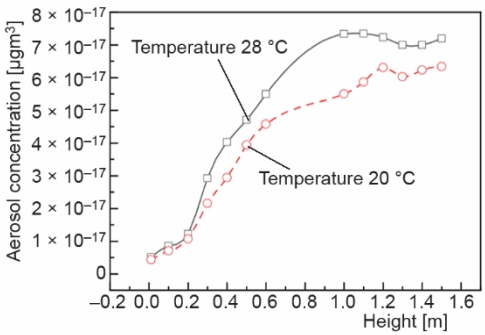

Figure 6. Variation of spatial aerosol concentration with altitude

As illustrated in fig. 5, within the designated vaccination area, aerosols manifest a pronounced deposition tendency, with a portion of the aerosol particles gradually descending to the ground due to gravitational forces, while others are transported by air currents towards the upper regions of the carriage. In the observation area, aerosol distribution is primarily concentrated in the middle part of the carriage, with a relatively limited range of diffusion. Aerosols exhibit a reduced distribution within the transition zone. Figure 6 illustrates the variation of aerosol concentration in space with altitude under conditions of 20 ℃ and 28 ℃. As altitude increases, the aerosol concentration in space concomitantly rises, with the highest recorded aerosol concentration occurring at a height of 1.5 m from the bottom of the carriage, measuring 7.2×10^{-17} micrograms per cubic meter. Consequently, as the temperature rises, the dispersion of aerosols in space becomes more pronounced. This phenomenon is primarily attributable to the rise in temperature, which accelerates the speed of air molecules. Consequently, aerosol particles become more readily dispersed in the atmosphere.

Temperature characteristics of different tube types

The analysis results indicate that the effectiveness of heat transfer varies among different tube shapes, including circular, square-round, and hexagonal. Figure 7 presents a schematic representation of the pressure variation for three distinct types of tubes. Figure 8 presents a chart illustrating the variation in temperature among three distinct tube types.

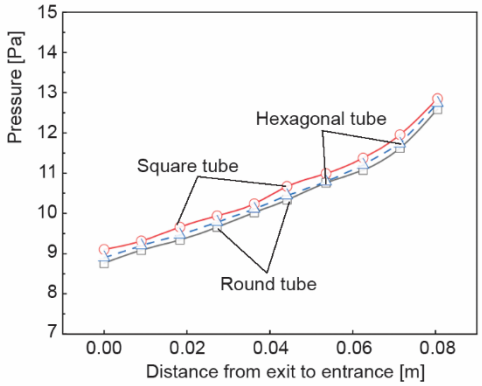

Figure 7. Pressure variation diagram

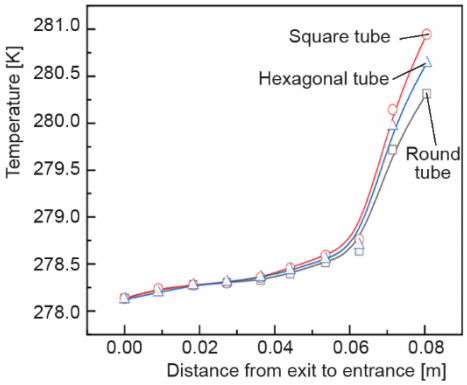

Figure 8. Temperature variation chart

As demonstrated in fig. 7, the rate of fluid pressure change within the square tube is more significant in comparison to the hexagonal tube. Concurrently, the fluid temperature within the circular tube appears to undergo the most gradual change, exhibiting a stable and uniform pressure fluctuation. In the range of 0-80 mm, the rate of pressure change in each tube exhibited a uniform and stable growth trend, with the pressure value gradually increasing from an initial 9-11 Pa. However, when the distance increased to 70-80 mm, the rate of pressure change within the tubes began to accelerate, with the pressure in all three tubes rising by approximately 1 Pa during this stage. The aforementioned phenomenon can be explained as such: with the flow of fluid within the pipe, internal disturbance factors gradually accumulate and intensify, which in turn leads to an acceleration of the rate of pressure change within the pipe.

As illustrated in fig. 8, a simulation analysis was conducted to examine the temperature variations within circular, square-round, and hexagonal tubes. It has been observed that as the distance from the outlet to the inlet increases, the temperature of the fluid gradually rises. The temperature variation trend exhibited by the three types of tubes remains consistent. Subsequent analysis indicates that the temperature change rate of the fluid within the square-round tubes is more substantial in comparison to the hexagonal tubes, while the temperature variation of the fluid within the circular tubes manifests as the most gradual. Within the range of 0-60 mm, the temperature variation of the fluid inside three types of pipes demonstrates a high degree of similarity. In the initial stage (0-40 mm), the fluid temperature inside each pipe type remains constant at 278.15 K. As the distance increases, the fluid temperature begins to rise slowly, and by about 40 mm, the temperature has approached 278.3 K. Subsequently, within the range of 40-60 mm, the rate of temperature increase gradually accelerates, and the trend of change becomes more pronounced, with the fluid temperature steadily rising to about 278.6 K. When the distance extends to 60-70 mm, the rate of temperature change reaches its peak.

Effect of fin spacing on heat transfer (vaccination area and observation area)

Figure 9 presents the change of heat transfer and air side pressure drop at different fin spacing in the inoculation area. As demonstrated in fig. 10, the variation in heat transfer and the decline in airside pressure were observed at distinct fin heights within the designated observation area.

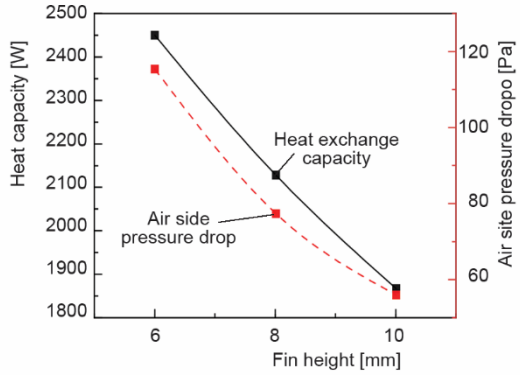

Figure 9. Heat transfer and air-side pressure drop variation with different fin spacings

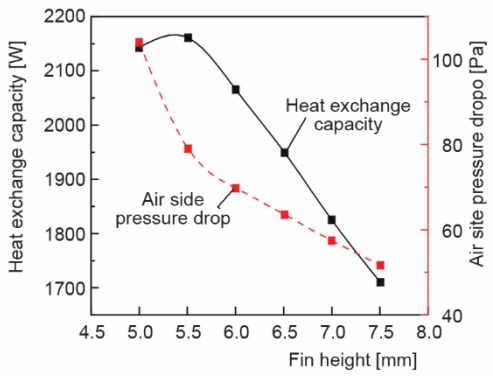

Figure 10. Heat transfer and air-side pressure drop variation with different fin heights

As illustrated in fig. 9, by simulating the changes in heat transfer rate and air-side pressure drop inside the circular tube under different fin spacings, the specific impact of different fin spacings on these two key parameters can be clearly determined. The findings of the study indicate a discernible downward trend in both the heat transfer rate and the air-side pressure drop as the fin spacing increases incrementally. In the context of the study, observations have been made concerning the phenomenon of heat transfer. It has been determined that when the fin spacing is configured at a distance of 6 mm, the rate of heat transfer attains its maximum value of 2452.5 W. Conversely, augmenting the fin spacing to 10 mm results in a decline in the rate of heat transfer, reaching a minimum of 1813.8 W. This observation une-

quivocally demonstrates the direct influence of fin spacing on the efficiency of heat transfer. In a similar vein, the simulation results pertaining to the airside pressure drop demonstrate a congruent pattern.

As demonstrated in fig. 10, the variation of heat transfer inside the circular tube and the air-side pressure drop in the observation area are contingent on the fin height. The findings of the study demonstrate a decrease in both heat transfer and air-side pressure drop with an increase in fin height. In the context of the study, observations have been made concerning the phenomenon of heat transfer. It has been ascertained that the fin height of 6 mm yields the highest value, reaching 2163 W. Conversely, when the fin height is increased to 10 mm, the heat transfer declines to its lowest value of 1711.5 W. The maximum air-side pressure drop is observed at a fin height of 6 mm, with a recorded value of 103.98 Pa. At a fin height of 10 mm, the air-side pressure drop reaches its lowest recorded value of 51.8 Pa. Fin spacing has been identified as a pivotal factor influencing air flow and heat exchange efficiency within epidemic prevention vehicles. This phenomenon is directly related to the spatial heat exchange effect within the vehicle. When the fin spacing is set correctly, it has been demonstrated to promote more uniform air flow inside the vehicle. In circumstances where air-flow is unobstructed, air filters have been shown to be capable of more efficaciously capturing aerosol pollutants in the atmosphere.

Effect of different fin spacing and height on indoor pollution characteristics

The spacing and height of the fins have been demonstrated to directly impact the air-flow characteristics and the process of heat exchange within the vehicle. It is imperative to note that adjusting these two parameters will have a direct impact on the performance of the heat exchanger. Consequently, this will affect the temperature distribution of the air inside the vehicle, thereby further influencing the spread of pollutants within the vehicle. As demonstrated in fig. 11, the study investigated the effect of different fin heights on the concentration of aerosols within the epidemic prevention vehicle. As illustrated in fig. 12, the effect of varying fin spacings on aerosol concentration within a pandemic response vehicle is demonstrated.

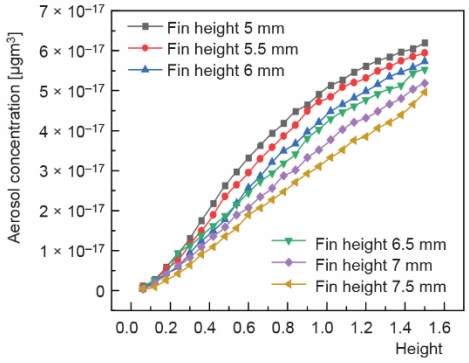

Figure 11. The effect of different fin heights on the aerosol concentration

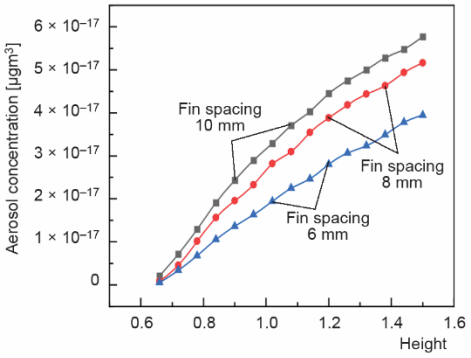

Figure 12. The effect of different fin spacings on the aerosol concentration

As demonstrated in fig. 11, the study investigated the effect of different fin heights on the concentration of aerosols within the epidemic prevention vehicle. The findings of the study demonstrate a discernible downward trend in the concentration of aerosols within the

vehicle as the height of the fins is increased incrementally. When the fin height is set at 5 mm, the maximum concentration of aerosols within the epidemic prevention vehicle can reach 6.1×10^{-17} μg/m^3. Conversely, at a fin height of 7.5 mm, the maximum aerosol concentration within the vehicle is 4.6×10^{-17} μg/m^3. This finding suggests that an increase in fin height may contribute to a reduction in the concentration of aerosols within the vehicle, which could in turn potentially decrease the risk of pathogen transmission in the air.

As illustrated in fig. 12, the effect of varying fin spacings on aerosol concentration within a pandemic response vehicle is demonstrated. The findings indicate a substantial decrease in the number of aerosol particles inside the vehicle with decreasing fin spacing. When the fin spacing is set at 10 mm, the aerosol concentration within the vehicle is measured at 6×10^{-17} μg/m^3. Conversely, when the fin spacing is reduced to 6 mm, the aerosol concentration recorded is 3.9×10^{-17} μg/m^3, which is approximately 1.5 times lower than the concentration observed at 10 mm fin spacing. This phenomenon can be explained by the fact that a smaller fin spacing significantly improves heat exchange efficiency, leading to increased temperature uniformity inside the vehicle, and thus a decrease in aerosol concentration. The findings suggest that decreasing the fin spacing may result in a reduction of aerosol concentration within the vehicle, which could lead to enhanced air quality and a reduction in the risk of virus transmission. Consequently, the selection of optimal fin spacing emerges as a pivotal aspect in the control of aerosol dispersion when conceptualizing and operationalizing pandemic response vehicles.

Conclusions

A growing body of research has demonstrated that shapes such as round, square--round, and hexagonal exhibit significant disparities in their respective heat distribution characteristics. The temperature of the fluid within the three types of tubes gradually increases with the increase in distance. The temperature change rate within the square tube is the most substantial, followed by the hexagonal tube, while the round tube demonstrates the most gradual temperature change. A reasonable spacing configuration is instrumental in achieving uniform air heat exchange. The reduction in fin spacing has been demonstrated to enhance the efficiency of heat exchange and decrease the concentration of aerosols within the epidemic prevention vehicle. This, in turn, has been demonstrated to enhance air quality and mitigate the risk of virus transmission.

The subsequent research endeavors will encompass the implementation of micro-electromechanical systems (MEMS) [12, 13] for the purpose of monitoring aerosol concentration, temperature, and humidity. The MEMS gas sensors have been demonstrated to possess the capability to accurately monitor the aerosol concentration inside a vehicle in real time [14]. The underlying working principle of these devices is predicated on the adsorption and reaction of specific gas molecules, which results in the generation of a detectable electrical signal change. In an epidemic prevention surveillance vehicle, such sensors can be installed in different areas, such as the vaccination area, observation area, and buffer zone. In the event of an abnormal increase in aerosol concentration, an alarm can be issued in a timely manner, thereby alerting the staff to take the necessary measures, such as strengthening ventilation and disinfecting relevant areas. This approach is effective in reducing the risk of virus transmission. The MEMS temperature and humidity sensors [15] have been demonstrated to achieve precise measurements of temperature and humidity within the vehicle. In the context of an epidemic prevention surveillance vehicle, the maintenance of optimal temperature and humidity conditions is paramount not only for the well-being of the occupants but also for the effective containment of

aerosol transmission and the seamless functioning of onboard equipment. Real-time temperature and humidity monitoring facilitates the prompt adjustment of the air conditioning system's operating parameters, thereby ensuring the stability of the indoor environment in terms of temperature and humidity. This, in turn, enhances the safety and efficacy of epidemic prevention efforts.

Acknowledgment

This work was supported by Changzhou University Science and Technology Cooperation Project (20240448) and the Modern Agricultural Science and Technology Innovation Special Fund Project of Jiangsu Province (BE2022426) and of China.

References

[1] Vucicevic, B. S., *et al.*, Impact of Lockdown on Air Quality in Belgrade During COVID - 19 Pandemic, *Thermal Science*, *28* (2024), 1B, pp. 557-567
[2] Dmitrasinovic, S. S., *et al.*, Traffic Intensity and Air Pollution before and during Lockdown in Novi Sad, Serbia, *Thermal Science*, *27* (2023), 3B, pp. 2333-2345
[3] Gul, N., *et al.*, COVID - 19 Modelling with Square Root Susceptible - Infected Interaction, *Thermal Science*, *27* (2023), Suppl 1, pp. S323-S332
[4] Wan, Q, *et al.*, Optimization of a Localized Air Conditioning System Using Thermoelectric Coolers for Commercial Vehicles, *Journal of Electronic Materials*, *46* (2017), Nov., pp. 2990-2998
[5] Zhang, H., *et al.*, Studies of Air-Flow and Temperature Fields inside a Passenger Compartment for Improving Thermal Comfort and Saving Energy. Part I: Test/Numerical Model and Validation, *Applied Thermal Engineering*, *29* (2009), 10, pp. 2022-2027
[6] Luo, Q., *et al.*, Role of Pathogen-Laden Expiratory Droplet Dispersion and Natural Ventilation Explaining a COVID-19 Outbreak in a Coach Bus, *Building and Environment*, *220* (2022), 109160
[7] Yang, X., *et al.*, Transmission of Pathogen-Laden Expiratory Droplets in a Coach Bus, *Journal of Hazardous Materials*, *397* (2020), 122609
[8] Roache, P. J., Conservatism of the Grid Convergence Index in Finite Volume Computations on Steady - State Fluid Flow and Heat Transfer, *Journal of Fluids Engineering - Transactions of the ASME*, *125* (2023), 4, pp. 731-732
[9] Zou, K., *et al.*, A Multiobjective Particle Swarm Optimization Algorithm Based on Grid Technique and Multistrategy, *Journal of Mathematics*, *2021* (2021), 1626457
[10] Liu, H. L., *et al.*, Effects of Mesh Style and Grid Convergence on Numerical Simulation Accuracy of Centrifugal Pump, *Journal of Central South University*, *22* (2015), 1, pp. 368-376
[11] Yang, Y., *et al.*, Transport and Control of Droplets: A Comparison between Two Types of Local Ventilation Air-Flows, *Powder Technology*, *345* (2019), Mar., pp. 247-259
[12] He, J.-H., *et al.*, Modeling and Numerical Analysis for an MEMS Graphene Resonator, *Front. Phys.*, *13* (2025), 1551969
[13] He, J.-H., Periodic Solution of a Micro-Electromechanical System, *Facta Universitatis, Series: Mechanical Engineering*, *22* (2024), 2, pp. 187-198
[14] Hsueh, T. J., Lu, C. L., A Hybrid YSZ/SnO_2/MEMS SO_2 Gas Sensor, *RSC Advances*, *9* (2019), 48, pp. 27800-27806
[15] Xu, Wei, *et al.*, Monolithically Integrated Bidirectional Flow Sensor and Stacked Temperature/Humidity Sensor Based on CMOS - Compatible MEMS Technology, *IEEE Transactions on Instrumentation and Measurement*, *73* (2024) 7501609

Paper submitted: October 15, 2024
Paper revised: April 8, 2025
Paper accepted: May 22, 2025